Energy Advances

PAPER

View Article Online
View Journal | View Issue

Cite this: *Energy Adv.*, 2025, 4, 683

Electroactive phase dependent triboelectric nanogenerator performance of PVDF–TiO_2 composites†

Irthasa Aazem,[ab] Charchit Kumar,[d] Ryan Walden,[ab] Aswathy Babu,[ab] Amit Goswami,[ac] Steven J. Hinder,[e] Gaurav Khandelwal,[d] Daniel M. Mulvihill,[d] Gerard McGranaghan[ac] and Suresh C. Pillai *[ab]

Received 5th September 2024,
Accepted 9th March 2025

DOI: 10.1039/d4ya00525b

rsc.li/energy-advances

This investigation explores the impact of the electroactive phase of a well-known tribonegative polymer, polyvinylidene fluoride (PVDF), on its triboelectric behaviour by compositing it with anatase, rutile, and mixed-phase TiO_2 nanoparticles. PVDF–TiO_2 polymer composite films with TiO_2 having different crystalline phases were prepared by spin coating. TENG specimens were fabricated using the prepared films and tested for their TENG properties in contact separation mode by pairing them with ITO-coated PET substrates. The XRD and FT-IR results show that the TiO_2 nanoparticles with rutile phase imparted the highest percentage of β crystalline phase in PVDF compared to that of the anatase and mixed phase. The difference in surface roughness of PVDF–TiO_2 composites was also observed with the change in the crystalline phase of the incorporated TiO_2 nanoparticles in the polymer matrix. The TENG studies suggest that the PVDF incorporated with rutile TiO_2 shows the highest output voltage (peak–peak ~105 V at 60 N force) compared to all the other PVDF–TiO_2 composites at specified contact forces and frequencies, whereas PVDF incorporated with anatase TiO_2 and a mix of anatase and rutile TiO_2 showed peak–peak voltages of ~82 V and ~33 V respectively. These results offer insights into the crystalline phase-dependent triboelectric behaviour of polymers and the enhancement of their TENG performance through the tuning of polymer crystalline phases using fillers.

1. Introduction

The advancements in renewable energy technologies and the proliferation of sensor networks during recent years have laid the foundation for the steady progress of the internet of things (IoTs) and for achieving the sustainable development of mankind. Consequently, the number of so-called small and smart electronic devices such as sensors, wireless transmitters, actuators *etc.* installed across the globe and even wearable smart electronics has increased tremendously in the order of billions and trillions.[1–4] However, the limited life spans and environmental concerns associated with the energy-storing units for powering these electronics are still far from being addressed and indicate the need for self-powered electronics. Since their discovery in 2012[5] triboelectric nanogenerators (TENGs) have been an emerging area of research focused on self-powered electronics for diverse applications. TENGs can harvest the otherwise wasted energy from various forms of mechanical motion, such as human body movements and large-scale wind and ocean waves.[3] The mechanism of working of TENGs is based on a combination of contact electrification and electromagnetic induction. TENGs have shown distinctiveness compared to other energy harvesting systems owing to their straightforward fabrication methods,[6–8] high power density[9,10] and feasibility of hybridization with other energy technologies[11–13] *etc.* Recent research has validated TENG's capabilities as a reliable technology for next-generation electronics by demonstrating TENG-based electronic skin, flexible and touch-screen displays, electronic watches, biomechanical monitoring sensors, *etc.*[4,14,15]

Current research is more focused on new designs and strategies for generating higher power output from TENGs

[a] *Nanotechnology and Bio-Engineering Research Group, Department of Environmental Science, Atlantic Technological University, ATU Sligo, Ash Lane, Sligo F91 YW50, Ireland. E-mail: Suresh.Pillai@atu.ie, Irthasa.AazemVS@research.atu.ie*
[b] *Health and Biomedical (HEAL) Strategic Research Centre, Atlantic Technological University, ATU Sligo, Ash Lane, Sligo F91 YW50, Ireland*
[c] *Department of Mechanical and Manufacturing Engineering, Atlantic Technological University, Ash Lane, Sligo F91 YW50, Ireland*
[d] *Materials and Manufacturing Research Group, James Watt School of Engineering, University of Glasgow, Glasgow G12 8QQ, UK*
[e] *The Surface Analysis Laboratory, Faculty of Engineering and Physical Sciences, University of Surrey, Guildford, Surrey GU2 7XH, UK*

† Electronic supplementary information (ESI) available. See DOI: https://doi.org/10.1039/d4ya00525b

and on experimenting with new materials for higher efficiency. However, further investigation is required to gain a deeper understanding of the factors contributing to TENG properties, beyond just the magnitude of the output produced. Polymer composites have been extensively studied as a promising material for TENGs.[16] Among them, polyvinylidene fluoride (PVDF) and its composites have been extensively studied in recent times to explore its excellent tribonegative behaviour. It has been demonstrated to be a promising material for TENGs.[16,17] Several factors such as the dipole moment, beta crystalline phase and the presence of highly electro-negative fluorine, *etc.* are being pointed out as the reason for this.[18,19] Also, among the various PVDF-based polymer composite films that have been explored so far for TENGs, reinforcing PVDF with TiO_2 has been shown to have a considerable enhancement in the output.[20,21] Various dielectric nanoparticles have been composited with PVDF to enhance the triboelectric properties of this polymer to be used in TENGs. PVDF–$CoFe_2O_4$,[17] PVDF–active carbon (AC@PVDF),[18] PVDF–graphene nanosheets[19] *etc.* are some of the PVDF-based composites explored recently other than TiO_2 incorporated PVDF. It has been proven that the incorporation of TiO_2 enhances the tribonegative property of the PVDF matrix by increasing the percentage of electroactive phase present in PVDF. Even though many studies on PVDF–TiO_2-based TENGs have already been reported, to the best of our knowledge there are no reports on the impact of crystallinity and the crystalline phases of TiO_2 on the TENG performance of PVDF–TiO_2 composites. The increase in the dielectric constant of PVDF–TiO_2 composites with the crystallinity of TiO_2 is reported.[22] Moreover, the TiO_2 when subjected to heat treatment undergoes a phase change and change in crystalline size, which eventually leads to a phase transformation in the polymer matrix to which it is incorporated.[23,24] Considering these factors, it is worthwhile to investigate how the crystalline phase of TiO_2 impacts the crystalline phases present in a semicrystalline polymer like PVDF which is highly sensitive to phase changes assisted by nanoparticles or fillers and how it is reflected in the TENG performance of the composite material. Moreover, the difference in crystallinity of TiO_2 may also have an influence on the surface topography of the PVDF–TiO_2 composite films, which would affect their triboelectric property.

Herein, we have investigated the change in the triboelectric behaviour of PVDF in response to modifications in their crystalline phase and electroactive phase content, assisted by TiO_2 nanoparticles with different crystalline phases. TiO_2 was chosen as the filler for this study as it exhibits a change in crystalline phase subjected to high-temperature calcination. Synthesized TiO_2 nanoparticles were calcined at different temperatures ranging from 400 °C to 900 °C. This yielded TiO_2 samples with a range of different crystalline natures, which were then incorporated into the PVDF matrix and thin films were prepared by spin coating. The change in crystalline phases and crystallite size in TiO_2 nanoparticles with calcination temperature was analysed using XRD. FT-IR analysis of the composite films rendered information on the percentage of different electro-active phases of PVDF present in these composites. Furthermore, the composite films showed the difference in percentage crystallinity in PVDF by incorporating TiO_2 with different crystalline phases. The SEM images and 3D profilometry data of the composite films showed the difference in surface topography of the films mainly focusing on the surface roughness. TENG specimens were fabricated from these films by attaching Cu tape as back electrodes. The TENG studies of the fabricated specimens were carried out by contacting them with a commercially purchased ITO-coated PET substrate at different forces and frequencies. The results indicated that the crystalline phase of TiO_2 has a significant influence on modulating the phase characteristics of PVDF. This has a profound role in enhancing the triboelectric properties of the TENG. This work is expected to deliver direction to tune up the TENG performance of polymers based on the crystalline phase of the fillers incorporated in them.

2. Experimental section

2.1. Chemicals and reagents

Titanium tetraisopropoxide (97%) and 2-propanol ($\geq$99.5%) were purchased from Sigma Aldrich. Polyvinylidene fluoride (PVDF) was purchased from Fisher Scientific. Acetone was purchased from Merck and dimethyl formamide (DMF) was purchased from Fisher Scientific. All chemicals and reagents were used without further treatment or purification.

2.2. Synthesis of TiO_2 nanoparticles

A typical sol–gel process was utilized to synthesize TiO_2 nanoparticles.[25–27] The precursor solution consisting of titanium tetraisopropoxide ($Ti(OPr)_4$) and 2-propanol ($(CH_3)_2CHOH$) was prepared first. For this, 46.8 mL $Ti(OPr)_4$ was added to 400 mL of 2-propanol and vigorously stirred at room temperature for 10 minutes. To this, 70 mL of deionized (DI) water was added, and the reaction mixture was allowed to stir vigorously for 2 h to improve the homogeneity and stability of the slurry. The sol formed was transferred into an oven set and heat treated at 80 °C for 24 h for ageing. The powder obtained was calcined at target temperatures of 400 °C, 500 °C, 600 °C, 700 °C, 800 °C, and 900 °C for 2 h at a heating ramp rate of 5 °C min^{-1} in a muffle furnace to obtain TiO_2 nanoparticles with different crystallinity. Samples were designated as TiO_2 400, TiO_2 500, TiO_2 600, TiO_2 700, TiO_2 800, and TiO_2 900. The calcination of synthesized TiO_2 nanoparticles at different temperatures was carried out at identical heating conditions by placing them in crucibles having the same dimensions and placing them in crucibles with the same dimensions and the same quantity of samples. This was important to make sure the samples were in a good position for comparison as the dimensions of the crucible and the quantity of the samples taken, affect the crystallinity of the calcined samples.

2.3. Preparation of PVDF–TiO_2 polymer composite films by spin coating

TiO_2-incorporated PVDF nanocomposite films were prepared by spin-coating as shown schematically in Fig. 1(a). The

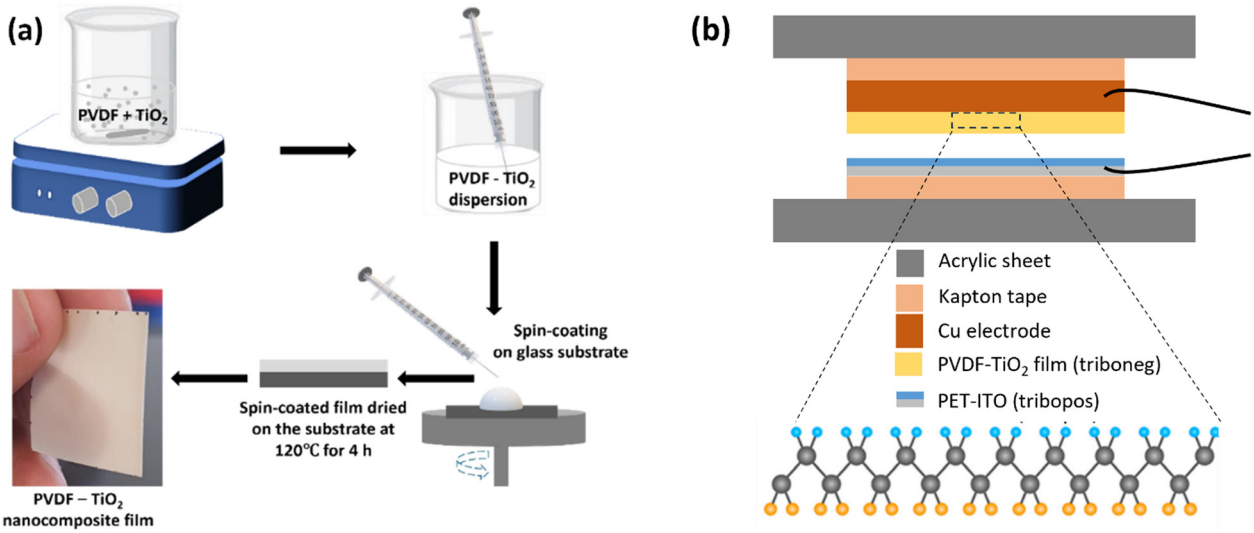

Fig. 1 Schematic representation of (a) the preparation of PVDF–TiO_2 nanocomposite films by spin coating and (b) the design of the fabricated TENG device.

TiO_2–PVDF films with TiO_2 nanoparticles calcined at different temperatures were prepared by first dispersing a required concentration of TiO_2 in 1 : 1 dimethyl formamide (DMF) and acetone solution. The particles were allowed to disperse uniformly for 24 h. Then PVDF (16.5 wt%) was added to this solution slowly over 30 minutes under constant stirring at 60 °C to avoid viscosity buildup and ensure homogeneity during the polymer dissolution in the solvent. The solution was stirred for 5 h to obtain a homogeneous polymer filler solution. After that, the solution was coated on a glass substrate by spin coating. For this ~1 mL of the homogeneous solution was added onto a 5 cm^2 clean and flat glass plate placed on the spinning chuck of the spin coater. All the film samples were prepared by coating at a spin speed of 1000 rpm for 35 s at room temperature (RT). The solution was uniformly coated over the glass plate after spinning. The films were then placed in a hot air oven at 120 °C for 4 h for complete drying. Freestanding films with approximately uniform thickness and smooth surfaces were obtained and stored for other characterizations and testing. PVDF film with no TiO_2 was also prepared using the same method. The PVDF film with no TiO_2 was designated as sPVDF and films containing TiO_2 were designated as PVT500, PVT600, PVT700, PVT800 and PVT900 based on the type of TiO_2 added. The solution preparation and spin coating parameters of the films were optimized through several trial-and-error experiments keeping the content of PVDF constant at 16.5 wt%. However, the viscosity build-up observed when adding 16.5 wt% of PVDF to the TiO_2 dispersed solution with TiO_2 content higher than 3 wt% indicates an important practical limitation in selecting the optimum TiO_2 percentage to get the best TENG output.

2.4. Fabrication of specimens for TENG testing

Spin-coated PVDF and PVDF–TiO_2 films (tribonegative layers) were cut into pieces with dimensions of 2.5 cm × 2.5 cm. Care was taken to eliminate any raised edges in the spin-coated films to avoid the possibility of restricting the contact between the surface of materials during TENG testing. Conductive copper tape was attached as the back electrode to one side of all the films. The electrodes were then insulated using Kapton tape. Thin conductive copper lead wires were drawn out from the copper electrode to capture the output signals from the TENG during testing. ITO-coated polyethylene terephthalate (PET) (tribopositive layer) was used as the second contact layer. A schematic representation of the TENG is shown in Fig. 1(b).

2.5. Material characterization

An X-ray diffractometer (Siemens D500) was used to analyse the crystalline structure and phase of TiO_2 nanoparticles and PVDF–TiO_2 nanocomposite films. The diffractometer utilized a Cu Kα radiation (λ = 0.15418 nm) at 40 kV and 30 mA for recording the XRD patterns at the 2θ range 10°–80° with a scan rate of 0.2° s^{-1}. Fourier transform infrared spectroscopy (FT-IR) analysis of the polymer composite samples was performed to evaluate the electroactive phase content of the polymer films. A PerkinElmer spectrometer (Spectrum 100) was utilized for this, and the spectra were obtained in the region 1500–600 cm^{-1}. X-Ray photoelectron spectroscopy (XPS) was employed to analyse the elemental composition and bonding characteristics of TiO_2 nanoparticles. XPS, Thermo Fisher Scientific, (East Grinstead, UK) K-Alpha+ spectrometer was used for obtaining the XPS data. The surface topography of the films was analysed from SEM scans obtained using the instrument FEI Nova NanoSem 630 and a 3D optical profilometer (Alicona InfiniteFocus).

2.6. TENG testing rig and electrical measurements

The TENG studies of the samples were carried out in vertical contact-separation mode. A high-precision linear electrodynamic testing machine (Electropuls E3000, Instron UK) was adapted as the test force impactor. At the actuation drive, a load cell having a capacity of 5 kN (tension and compression) was

equipped. A dedicated holder with a levelled base was utilised to achieve a parallel contact between the tribolayers. The bottom friction layer was fitted onto a 360° movable platform to ensure proper alignment for maximum contact between the test surfaces. The bottom tribo-layer position was locked to avoid any further movement while testing. Normal force of 20 N, 40 N and 60 N was applied at frequencies varying from 4 Hz to 8 Hz to obtain the electrical output from the different TENG devices. A separation distance of ~2 mm between the active layers was used during the measurements. The voltage signals from the TENG were recorded using a digital oscilloscope (RS PRO, Bench-top Mixed Signal Oscilloscope, UK). Current output was retrieved using a low-noise current amplifier (SR570, Stanford Research Systems, USA) and the signals were recorded on a digital oscilloscope. The output power from the TENG was measured under external load resistances ranging from 1 KΩ to 5 GΩ. All TENG testing was performed at ambient environment conditions.

3. Results and discussion

Synthesized TiO_2 nanoparticles were calcined separately at a range of temperatures from 400 °C to 1000 °C to obtain a gradual transition from anatase to rutile phase in TiO_2 with the change in calcination temperature. Utmost care was taken to avoid any chances of contamination in the TiO_2 synthesis by carrying out the reaction in a laminar flow hood. Moreover, the calcination of the TiO_2 powders carried out at higher temperatures (400 °C to 1000 °C) has also removed any impurity that would have been present in the sample. This was further ensured by analysing the XRD patterns of TiO_2 nanoparticles and confirming that no peaks other than TiO_2 peaks were present in the sample. Consequently, the impact of TiO_2 nanoparticles containing a single crystalline phase (anatase or rutile) and mixed-phase on altering the electroactive (EA) phase of the PVDF matrix in PVDF–TiO_2 composites can be evaluated and correlated with the TENG output of these samples. The preparation of PVDF–TiO_2 polymer solution was found to be smooth and convenient when the TiO_2 nanoparticles were dispersed fully in the solvent first and then added the polymer for dissolution. This is because, owing to the viscosity build-up in the polymer solution, a uniform dispersion of TiO_2 was difficult to achieve leading to particle agglomeration PVDF was dissolved in the solvent before the addition of TiO_2 in the initial trials of sample preparation. This will, in turn, hinder the effective interaction between the surface of TiO_2 particles and the single PVDF chains. The percentage loading of TiO_2 chosen for this study is not the optimized maximum loading for achieving the maximum TENG output.[20] There were practical limitations to increasing the loading of TiO_2 and PVDF above the amount used in this study as it led to viscosity increases in the PVDF–TiO_2 solution where the solution was unable to spin coat. By maintaining a constant speed and time of spin coating for all the prepared PVDF–TiO_2 samples, a consistent thickness of approximately 48 μm (Fig. S1 (ESI†)) was obtained for all the samples. The surface of the spin-coated film which was in contact with the glass base (coating substrate) appeared glossy, and the opposite exposed surface had a comparatively rough finish as expected. For fabricating the specimens for TENG testing, the surface with a rough finish (exposed surface) was considered the surface of interest for all the films. Therefore, the glossy surface was attached to the back electrodes. Considering the reliability of comparison between samples, it is important to use the same surface as the test surface for all the samples. This is crucial because TENG output is susceptible to the amount of real contact area developed between the materials and it varies considerably based on the nature of the materials' surface.[1,27] It is also worth mentioning that, as the comparison is between different TiO_2 crystalline phases, the percentage of TiO_2 in PVDF was kept constant for all the samples as the TiO_2 particles calcined at a range of temperatures were used in this study.

3.1. Material properties and crystalline phase analysis of TiO_2 nanoparticles and PVDF–TiO_2 films

Material characterization of the synthesized TiO_2 nanoparticles was carried out using X-ray photoelectron spectroscopic (XPS) and X-ray diffraction (XRD) analyses (Fig. 2). The XPS spectra of the TiO_2 nanoparticles were analysed to understand their elemental composition. Fig. 2(a) shows the survey spectra of the TiO_2 500, TiO_2 600, and TiO_2 900 samples. Peaks corresponding to titanium (Ti), oxygen (O) and carbon (C) were observed in the samples' survey spectrum. C 1s peaks were observed at binding energies of 285 eV in all the samples, which arise from contamination during synthesis and calcination of the nanoparticles. The two strong peaks from TiO_2 nanoparticles at around 465.2 eV and 459.5 eV (Fig. 2(b)) can be attributed to Ti $2p_{1/2}$ and Ti $2p_{3/2}$, respectively. These binding energies indicate that Ti is in a +4 oxidation state. Considering Ti's elemental composition and +4 oxidation state, it is reasonable to attribute the Ti–O bonding to TiO_2. Fig. 2(c) presents the XPS spectra of the O 1s of the TiO_2 samples. The peak positions of O 1s are located at 530.2 eV, which is in agreement with the reported O 1s electron binding energy for TiO_2.[26] The peak positions of Ti 2p which corresponds to the binding energy of Ti metal in TiO_2, O 1s which corresponds to the binding energy of oxygen in TiO_2 and a peak separation of 5.8 eV of the Ti 2p doublet agree well with the binding energy reported for TiO_2 nanoparticles.[26,27] Fig. 2(d) shows the percentage of elements present in each TiO_2 sample. XPS data identifies the presence of Ti–O bonding in the sample which confirms the formation of TiO_2 in all the particles and matches with the reported peak positions of Ti and O of TiO_2.[28] It is also worth mentioning that C, F and N are also observed (in Fig. 2(d)) in the samples due to contamination during the sample synthesis.

The identification of the crystalline phase of TiO_2 nanoparticles is crucial in the context of this study to assess the TiO_2 induced phase transformation in PVDF matrix and their effect on TENG output. XRD patterns of TiO_2 nanoparticles were analysed to investigate the crystallinity, crystal phases present and the change in crystallite size of the nanoparticles with an

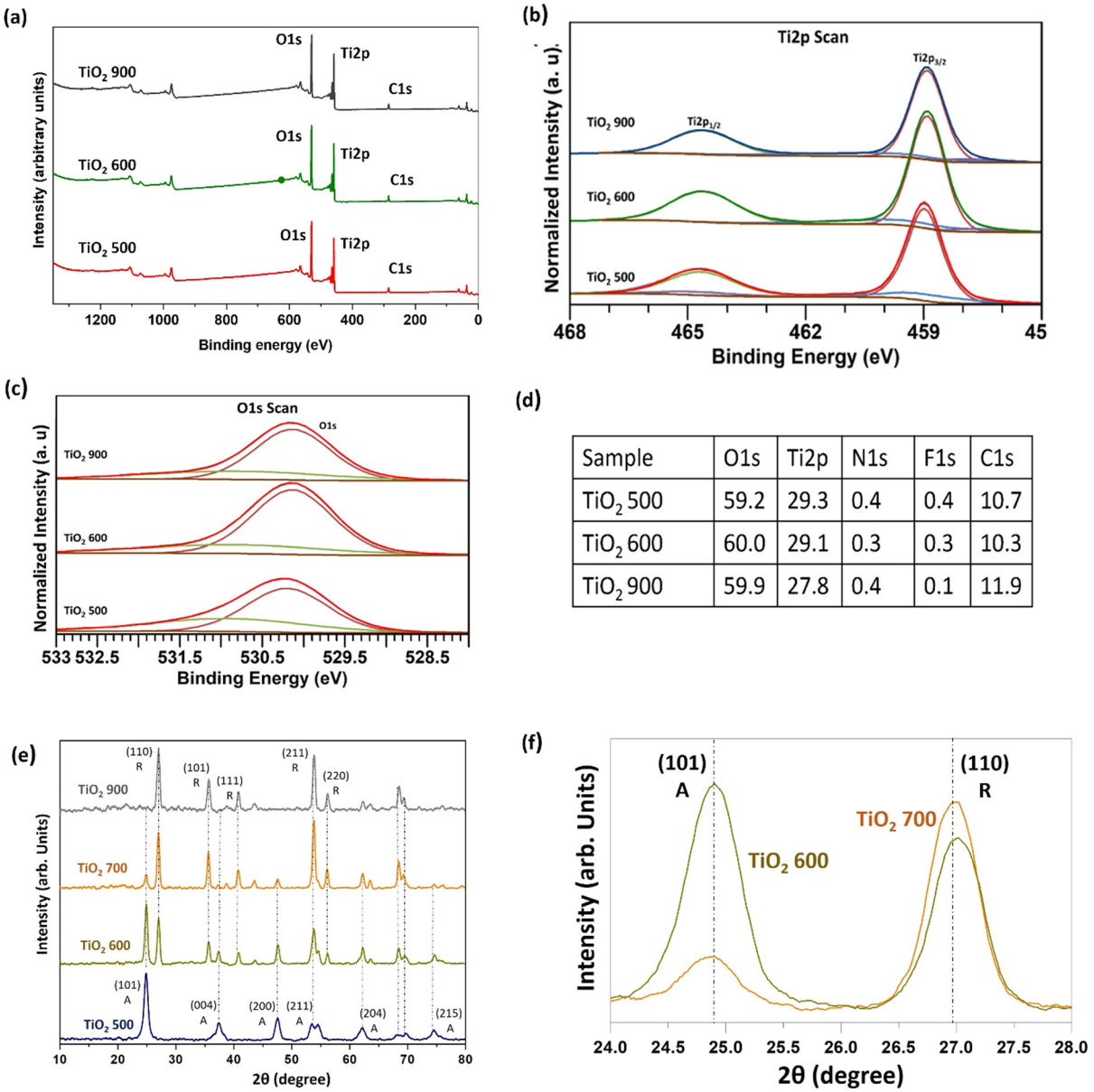

Sample	O1s	Ti2p	N1s	F1s	C1s
TiO_2 500	59.2	29.3	0.4	0.4	10.7
TiO_2 600	60.0	29.1	0.3	0.3	10.3
TiO_2 900	59.9	27.8	0.4	0.1	11.9

Fig. 2 XPS and XRD analysis of TiO_2 nanoparticles. (a) XPS survey spectra, (b) and (c) spectra of Ti 2p and O 1s BE region respectively and (d) tabulation of the composition of elements for TiO_2 500, TiO_2 600 and TiO_2 900. XRD patterns of TiO_2 showing (e) comparison of the patterns of TiO_2 500, TiO_2 600, TiO_2 700 and TiO_2 900 and (f) changes in the anatase (101) and rutile (110) peak intensities with change in calcination temperature from 600 °C to 700 °C.

increase in calcination temperature. The XRD patterns of synthesized TiO_2 nanoparticles calcined at different temperatures varying from 500–900 °C are shown in Fig. 2(e) and (f). Characteristic reflection peaks of the anatase phase of TiO_2 (JCPDS card no. 21-1272) were observed in TiO_2 500, TiO_2 600 and TiO_2 700 samples at $2\theta \sim 24.8°$, 37.4°, 47.5°, 53.5°, 62.1°, 68.4°, 69.6° and 74.6° corresponding to the Bragg's reflections from (101), (004), (200), (211), (204), (116), (220) and (215) crystal planes respectively.[27,29] Characteristic reflection peaks of the rutile phase of TiO_2 (JCPDS card no. 21-1276) were observed in TiO_2 700 and TiO_2 900 samples at $2\theta \sim 27.1°$, 35.6°, 40.8°, 53.9° and 56.2° corresponding to the *hkl* planes (110), (101), (111), (211) and (220) respectively.[27,29,30] The crystallinity of the materials is observed to increase with the increase in calcination temperature. This can be attributed to the enhancement in the definition of the crystalline phase by the reduction of defects, edges, strain, irregularities, *etc.* present in the particles due to heat treatment.[30,31] This can also be due to the transformation of the elongated side-to-side packed anatase phase to the closed packed octahedrally oriented rutile phase with increased calcination temperature.[31] The XRD pattern of TiO_2 500 shows that it is constituted of only the anatase phase of TiO_2. Whereas the XRD patterns of TiO_2 600 and TiO_2 700 samples show the presence of both anatase and rutile phases in these samples, but in different amounts, the XRD pattern of TiO_2 900 shows it is fully rutile. The crystallite

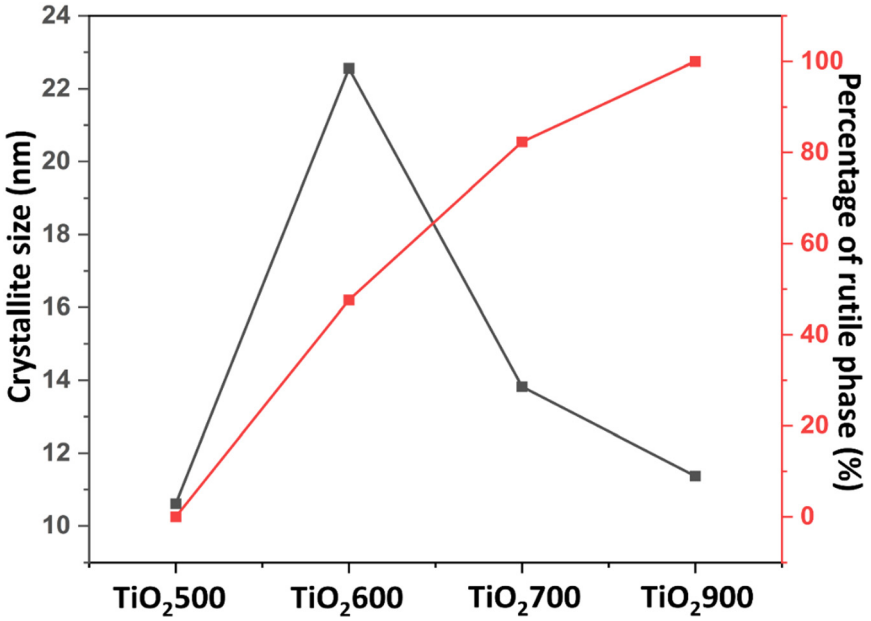

Fig. 3 Crystallite size and percentage of rutile phase of TiO_2 nanoparticles calcined at different temperatures.

size (φ) in nm, of TiO_2 nanoparticles was estimated by the Debye–Scherrer's equation (eqn (1))[26,32] as

$$\varphi = \frac{K\lambda}{\beta \cos\theta} \quad (1)$$

where φ is the crystallite size, K (0.9) is the shape factor, λ is the wavelength (1.5406 Å) of the X-ray used, β is the full width at half maxima (FWHM) of the peaks and θ is the Bragg's angle. From Fig. 3, which shows the estimated values of the crystallite size of the particles, it can be noted that the crystallite size of the particles increases with calcination temperature from 500 °C to 600 °C and then it reduces as the calcination temperature increases further up to 900 °C. This variation in crystallite size is due to the change in the percentage of anatase and rutile phases in the TiO_2 nanoparticles. TiO_2 600 has both anatase and rutile phases present in them which is the reason why TiO_2 600 has an increased crystallite size compared to that of TiO_2 500. TiO_2 700 also shows the presence of both anatase and rutile phases. However, its crystallite size is lower than that of TiO_2 600 as the percentage of anatase phase is considerably decreased in TiO_2 700 and it is in the process of getting converted to a single crystalline phase TiO_2. From this observation, it is clear that the presence of two different crystalline phases in TiO_2 results in an increase in their crystalline size compared to that of TiO_2 with only one crystalline phase. The percentage of anatase and rutile phases present in TiO_2 600 and TiO_2 700 (Fig. 3) were calculated by considering the intensities of anatase (101) and rutile (110) using the Spurr equation (eqn (2))[33] as

$$F_R = \frac{1}{1 + 0.8[I_A(101)/I_R(110)]} \quad (2)$$

where F_R is the fraction of the rutile phase in the TiO_2 sample, I_A (101) is the intensity of (101) peak of the anatase phase and I_R (110) is the intensity of (110) of the rutile phase.

According to the Spurr equation, it was calculated that the percentage of the anatase phase is 52.4% and that of the rutile phase is 47.6% in the TiO_2 600 sample, and the percentage of the anatase phase is 17.7%, and that of the rutile phase is 82.3% in TiO_2 700 sample. The percentage of the anatase phase is reduced compared to that of the rutile phase as the calcination temperature is increased. On increasing the calcination temperature further from 700 °C to 900 °C it was found that the anatase phase has completely disappeared and TiO_2 900 contains only the rutile crystalline phase. From this, it can be inferred that the increase in calcination temperature favours the formation of a thermodynamically stable rutile phase. Also, the presence of both anatase and rutile phases in TiO_2 600 and TiO_2 700 shows that the phase transformation has taken place gradually.[29] XRD patterns of TiO_2 nanoparticles calcined at temperatures ranging from 400 °C to 1000 °C are shown in Fig. S2 (ESI†) to confirm that TiO_2 formation is not complete below 500 °C, there is no mixed phase present above 700 °C and both TiO_2 800 and TiO_2 1000 has only rutile phase.

Increasing the content of the electroactive phase (EA) in the PVDF matrix is crucial for many applications.[19,34] Similarly, the TENG output of PVDF could also be impacted by the percentage of different electroactive phases present in PVDF. FT-IR analysis is widely used to identify the percentage of crystalline phases present in PVDF.[35,36] FT-IR analysis of PVDF and PVDF–TiO_2 films (designated as PVT) with TiO_2 having different crystalline phases was carried out to evaluate the changes in the crystalline phase of PVDF and their percentage with the incorporation of TiO_2. Since the spin coating parameters for all the prepared films were the same (Section 2.3), the comparative changes observed in the electroactive phases in PVDF between the films

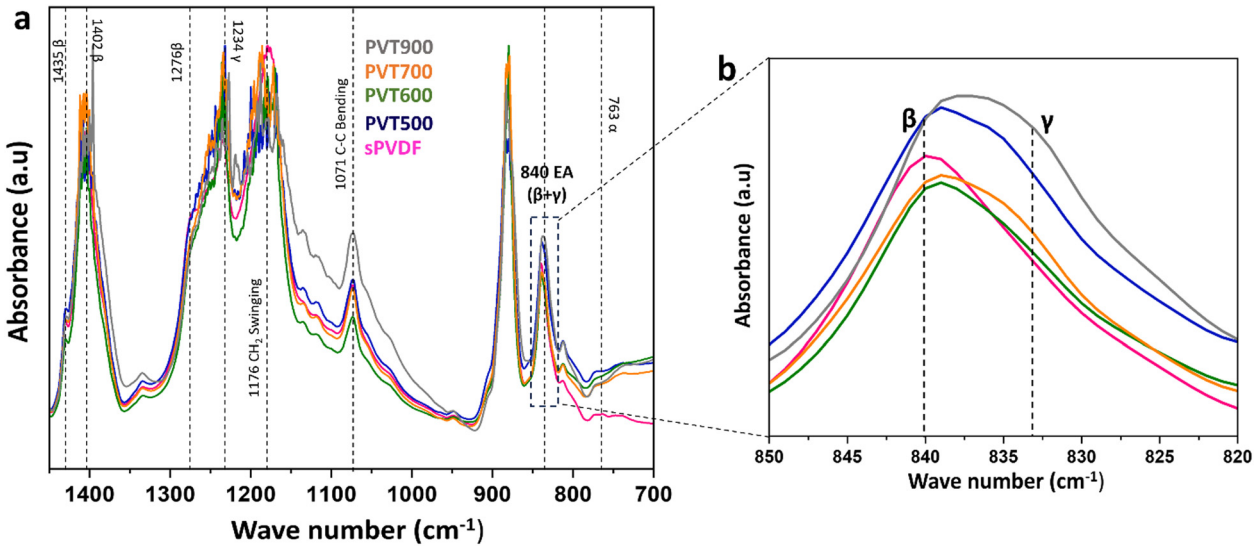

Fig. 4 FT-IR analysis of PVDF–TiO_2 composites. Comparison of FT-IR spectra (absorbance *vs.* wavenumber) tested in the range of (a) wavenumber 1450–700 cm^{-1} and (b) wavenumber 850–820 cm^{-1} of sPVDF, PVT500, PVT600, PVT700 and PVT900.

can be attributed to the influence of TiO_2 particles. Fig. 4(a) and (b) compare the FT-IR spectra of PVDF and PVDF–TiO_2 composites. The peak observed at 1071 cm^{-1} corresponds to the bending vibration of C–C, the peak at 1176 cm^{-1} corresponds to the swinging vibration of CH_2 and the peak at 1397 cm^{-1} is due to CF_2 in PVDF.[37] The intensification of the vibration band at 1232 cm^{-1} for PVDF–TiO_2 films shows the nucleation of β crystalline phase in PVDF with the incorporation of TiO_2. Also, the absence of identity peaks of the α phase of PVDF at 763 cm^{-1} and 976 cm^{-1} in the spectra is an indication of the conversion of the α phase to electroactive phases (β and γ) of PVDF. Also, the peaks at 1276 cm^{-1} and 1402 cm^{-1} are assigned to the β phase and the one at 1234 cm^{-1} is attributed to the γ phase. Another major peak observed at 840 cm^{-1} is considered the electroactive phase of PVDF since it is a combination of both β and γ phases and correlated with the intensities of the peaks at 1276 cm^{-1} and 1234 cm^{-1}.[21,35,38] For this, the percentage of electroactive phase present in each sample was calculated from the FT-IR spectra using eqn (3)[35] as

$$F_{EA} = \frac{A_{EA}}{\left(\frac{K_{840}}{K_{763}}\right)A_{763} + A_{EA}} \times 100\% \quad (3)$$

where A_{EA} and A_{763} are absorbances at 840 and 763 cm^{-1} respectively and the absorption coefficients at these wave numbers (K_{840} and K_{763}) are 7.7 × 10^4 and 6.1 × 10^4 cm^2 mol^{-1} respectively. The fraction of EA phases of PVT500, PVT600, PVT700 and PVT900 were calculated as 71.61%, 68.28%, 72.55% and 75.74% respectively. On comparing the spectra of PVDF–TiO_2 samples with that of PVDF, it can be observed that the intensity of electroactive phases in PVDF is increased. This shows that incorporating TiO_2 into the PVDF matrix favours the formation of more electroactive phases in PVDF. Furthermore, since the TiO_2 nanoparticles incorporated into the PVDF matrix occur in different crystalline phases (as explained in the XRD analysis), a more detailed analysis of FT-IR is required to understand how the crystalline phase of TiO_2 impacts the phase transformation in PVDF. Fig. 4(b) shows that the peak at 840 cm^{-1} which corresponds to the EA phase of PVDF is widening with the incorporation of TiO_2 nanoparticles with different crystalline phases. This is a clear indication of the change in the EA phase of PVDF with the addition of TiO_2 and also that the crystalline phase of TiO_2 affects how the EA phase of PVDF–TiO_2 is being manipulated. A shift in the peak towards the lower wave number is observed in Fig. 4(b) and this shows the increase in the contribution of the γ phase in the EA phase which is a mixture of β and γ phase.[35,39] The intensification of the peak at 840 cm^{-1} can also be attributed to the enhancement of γ phase.[39] Fig. 4(b) shows that the γ content is higher for films containing full rutile (PVT900) and fully anatase (PVT500) and comparatively lower for PVT films containing mixed-phase TiO_2 (PVT600 and PVT700). However, the percentage of γ phase is the highest for PVT900.

XRD patterns of spin-coated PVDF film and PVDF–TiO_2 nanocomposite films (Fig. 5(a)–(c)) were analysed to understand the crystalline phase of the PVDF in them. Fig. 5(a) and (b) compares the XRD patterns of PVDF in powder form and spin-coated PVDF film. The two intense peaks observed in PVDF powder at 18.70° and at 20.20° and the medium peak at 26.5°, which corresponds to (020), (110) and (021) planes, respectively, are the major peaks of the monoclinic α-crystalline phase of PVDF which is considered as the kinetically stable phase.[16,23,40] In the case of spin-coated PVDF, the intensity of XRD peaks reduced and the peaks got broadened and shifted towards the right to 20.50°. This shows the enhancement of the β-crystalline phase in spin-coated PVDF. This is an indication of the transformation of the α-crystalline phase to the β-crystalline phase in PVDF by spin coating and the drying of samples at 120 °C. XRD peaks of both PVDF and TiO_2 are observed in Fig. 5(c) which shows the XRD patterns of all the

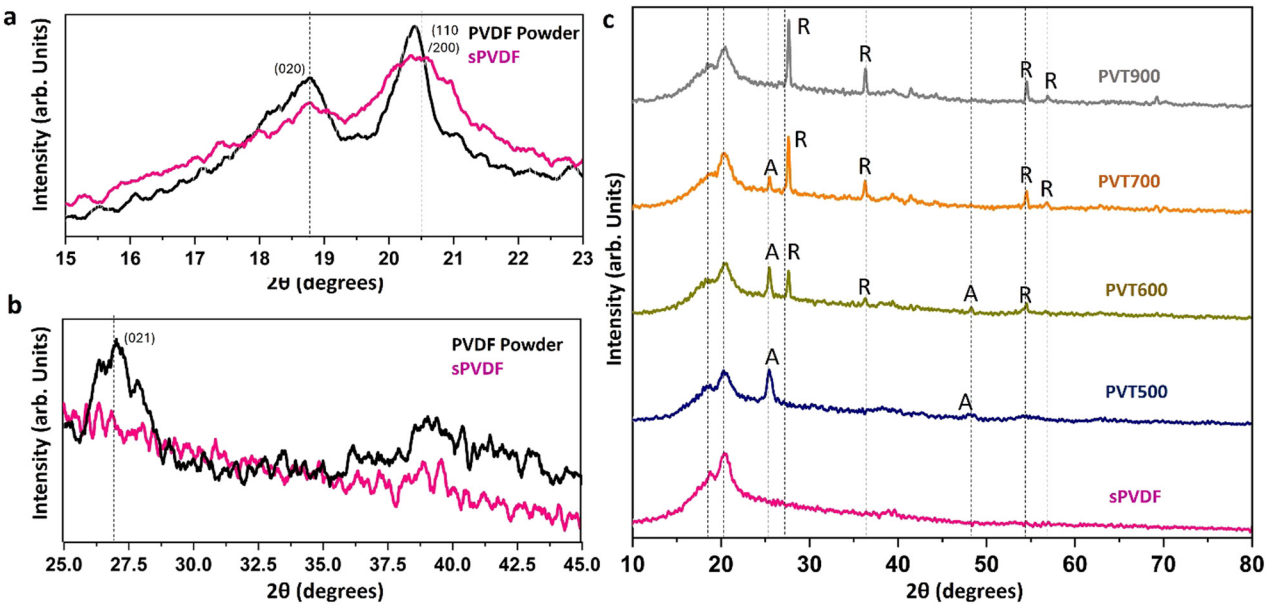

Fig. 5 XRD analysis of PVDF and PVDF–TiO_2 composite films. (a) and (b) Comparison of XRD patterns of PVDF powder and spin-coated PVDF (sPVDF) and (c) comparison of XRD patterns of sPVDF, PVT500, PVT600, PVT700 and PVT900.

PVDF–TiO_2 nanocomposite films prepared by spin coating. All the PVDF–TiO_2 composites have the same mass loading of TiO_2 (3 wt%). The presence of anatase and rutile phases in TiO_2 is also reflected in these XRD patterns of PVDF–TiO_2 composites. It can be observed that with the addition of TiO_2 in PVDF, the intensity of the (110/200) peak corresponding to the β-crystalline phase reduces showing further enhancement of the β-crystalline phase.[41] Also, with the incorporation of TiO_2, a reduction in crystallinity and enhancement of amorphous regions in PVDF is observed owing to the interaction of polymer chains with TiO_2 nanoparticles.[40] Fig. 6 shows the comparison of the XRD pattern of the PVT films in the 2θ range 15°–30°. It can be observed that the intensity of the major peak of PVDF at 20.5° is similar for PVDF, PVT500 (anatase) and PVT600 (anatase and rutile). Whereas the intensity of this peak is considerably decreased in the case of PVT900 (fully rutile). This shows that the TiO_2 nanoparticles with rutile crystalline phase impart more enhancement of the PVDF β-crystalline phase than other TiO_2 nanoparticles.

3.2. Surface topography analysis of PVDF–TiO_2 nanocomposite films

SEM scans and 3D profilometry images of PVDF and PVDF–TiO_2 films were analysed to observe the surface morphology of the films and to understand the distribution of TiO_2 nanoparticles in the PVDF matrix in these films. The surface scans of the PVT500, PVT600 and PVT900 from a 3D optical profilometer and their SEM scans are shown in Fig. 7(a)–(f). It can be

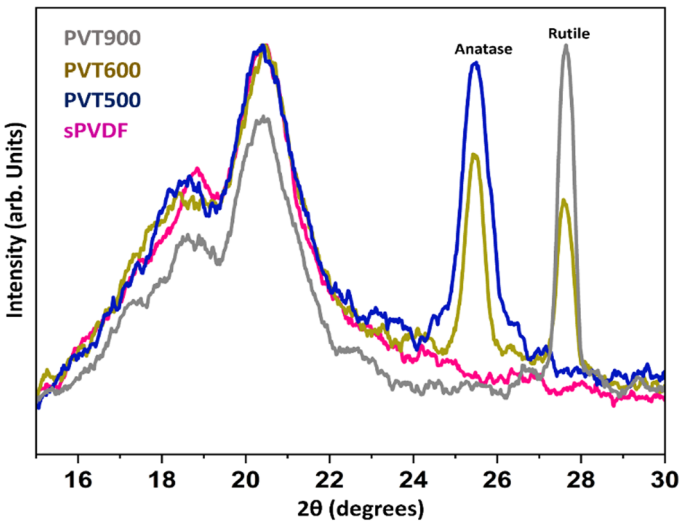

Fig. 6 Comparison of XRD patterns of sPVDF, PVT500, PVT600 and PVT900 in the 2θ range 15°–30°.

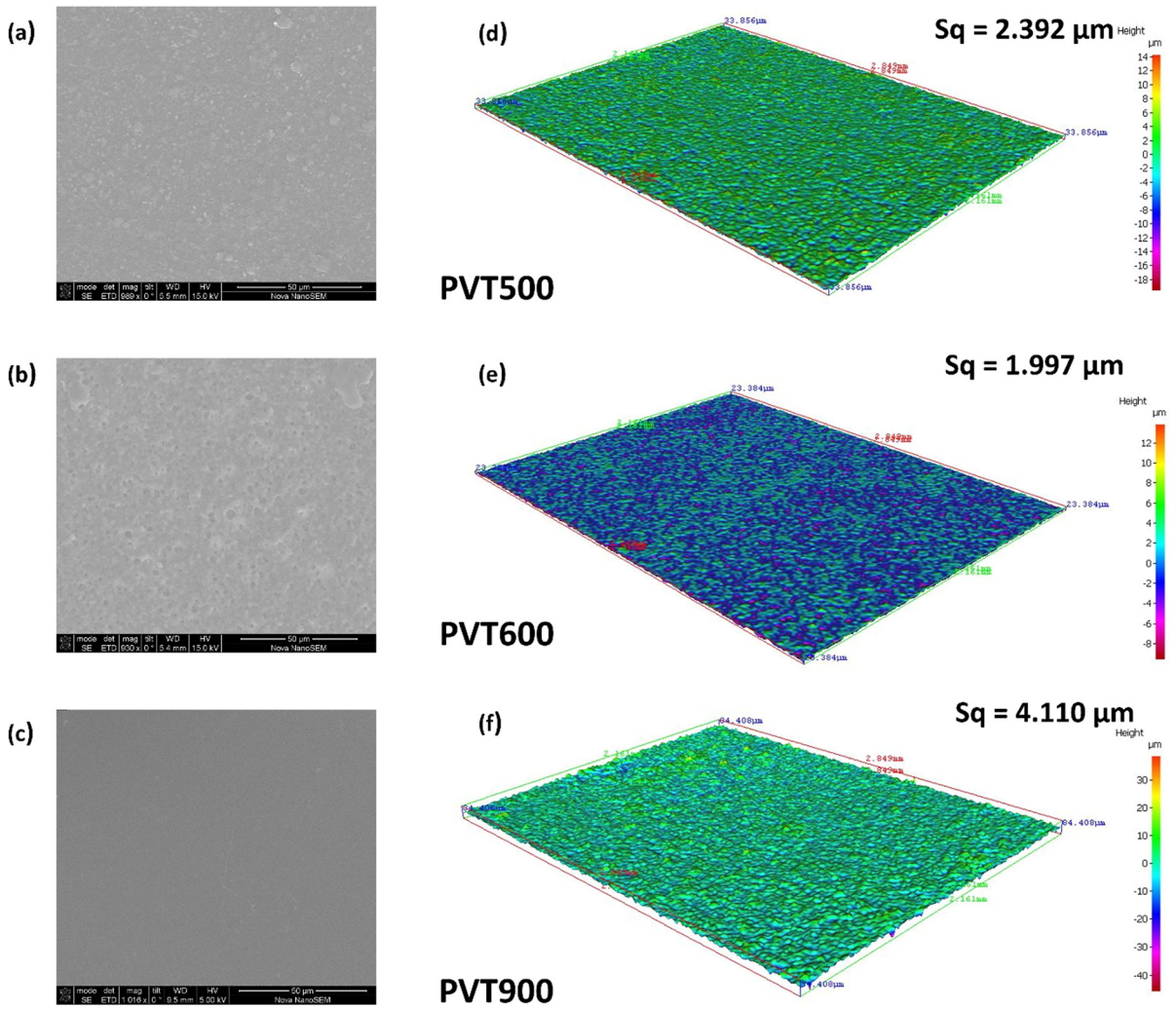

Fig. 7 SEM images (a–c) of the PVT500, PVT600 and PVT900 films and their surface scans (d–f) from a 3D optical profilometer.

observed that the roughness of the surface of the PVT900 film is higher than that of the PVT500 and PVT600 film. PVT900 shows a root mean square (RMS) surface roughness of 4.110 µm, which is higher than the S_q 1.997 µm and 2.392 µm of PVT600 and PVT500 respectively. This can be again correlated to the influence of crystallinity and crystallite size of the TiO_2 nanoparticles incorporated in these films. Since the average crystallite size of rutile TiO_2 is higher than that of the anatase TiO_2, the surface roughness of PVT900 is more than that of PVT600. Also, the RMS surface roughness of PVT500 falls in between that of PVT600 and PVT900. Fig. S3 (ESI†) shows the SEM scans of drop-casted and spin-coated PVDF films. On comparing the images of PVDF, spin-coated film and PVDF drop-casted films it can be observed that the spin-coated films show a more smooth and oriented film surface compared to that of drop-casted PVDF film. This can be an indication of the presence of a more crystalline phase than the amorphous phase in spin-coated PVDF compared to that of drop-casted PVDF film. Beta crystalline phase is reported to be favourable for triboelectric properties of PVDF compared to other crystalline phases.[20,42] From Fig. S4 (ESI†), TiO_2 nanoparticles embedded in the PVDF matrix are observed. It can be noted that the crystal size of TiO_2 embedded in the PVDF matrix is increasing with an increase in calcination temperature which agrees with the trend in crystallite size of TiO_2 nanoparticles estimated from their XRD patterns. Moreover, a homogeneous distribution of TiO_2 nanoparticles with a minimum agglomeration of reinforced particles is obtained in all the PVDF–TiO_2 films. This could be due to the overnight high-speed magnetic stirring employed to disperse the TiO_2 samples in PVDF solution. Moreover, the concentration of PVDF in the solution and the percentage loading of TiO_2 which was optimized for maintaining the uniformity of polymer nanocomposite was appropriate to achieve uniform distribution of the TiO_2 nanoparticles in the PVDF matrix. The SEM scans of PVDF and PVDF–TiO_2 samples clearly show the change in surface morphology of PVDF film with a change in crystallinity of the incorporated TiO_2 nanoparticles. It is visible that the surface roughness of the PVDF film is increasing compared to that of pristine PVDF film, with the incorporation of TiO_2 nanoparticles.

3.3. Triboelectric properties of PVDF–TiO_2 nanocomposite films

Tribo-electric properties of the PVDF–TiO_2 films were evaluated under contact separation mode with ITO-coated PET (PET) as the opposite triboelectric layer. The TENG test rig (Section 2.6) was designed and adjusted to ensure maximum contact between the triboelectric layers and negligible chances for the separate deformation or flexing of the individual layers. Also, it ensures that the output from the electrical testing is a result of the triboelectric (TE) effect due to the contact separation between the materials. The electrical output is a result of TE effect as the voltage output was measured across the two triboelectric layers when they were in continuous contact separation. There can be a contribution from the piezoelectric (PE) effect as well to the electrical output since PVDF is known for its piezoelectric properties. However, the contribution from PE effect can be negligible since there is another tribo-positive material (PET) involved in the contact separation. The electrical output contribution from PE effect under the contact-separation condition at 60 N for PVDF film was found to be only 0.15 V (Fig. S5 (ESI†)). The output voltage for the bare PVDF film and PVDF–TiO_2 nanocomposite films against (PET) was evaluated under 20 N, 40 N and 60 N contact force at 4 Hz, 6 Hz and 8 Hz frequencies. Fig. 8 shows the output voltage generated by pairing the prepared PVDF–TiO_2 composites with PET. Here, PVDF–TiO_2 film acts as the tribo-negative layer and the PET substrate acts as the tribo-positive layer. As expected, all samples showed an increase in the output voltage with an increase in the contact force and frequency. This is evident from Fig. 8(a)–(e). It is also expected that the electrical output signals (AC) may not be uniform and symmetric in the positive and negative cycle. This asymmetry is because of the nature of contact-separation between the materials which occurs from the operation of the testing device used. Therefore, there could be differences between the output signal generated during the contact cycles and during the separation cycles.[17,21,43] For the PVDF/PET pairing, the output voltage obtained was ~25 V. It increased up to ~60 V (2.4 times) for the PVT900/PET sample which was the highest voltage value obtained among all the samples. The increase in voltage value under the tested conditions with the incorporation of TiO_2 in the PVDF matrix confirms that the triboelectric properties of PVDF film are increased with the loading of TiO_2. However, the increase in voltage in PVDF–TiO_2 films was observed to be impacted by the crystalline phase of the TiO_2 in the PVDF matrix. Taking the example of the output values at 60 N and 8 Hz, the peak–peak voltage values obtained are ~35 V, 76 V, 33 V, 80 V and 105 V for PVDF, PVT500, PVT600 and PVT900 samples (Fig. 8(f)) respectively. The peak–peak voltage output of PVDF is doubled with the addition of anatase phase TiO_2 (PVT500) and it reduces considerably with mixed TiO_2 (PVT600) which has an almost equal percentage of anatase and rutile phase (Fig. 3). This can be attributed to the decrease in the beta crystalline phase observed in the PVT600 film compared to the other films. This can be also validated by the surface topography results obtained using the 3D profilometer. The PVT700 sample which also has a mix of anatase and rutile phases, but a considerably higher percentage of rutile than anatase, shows an increase in

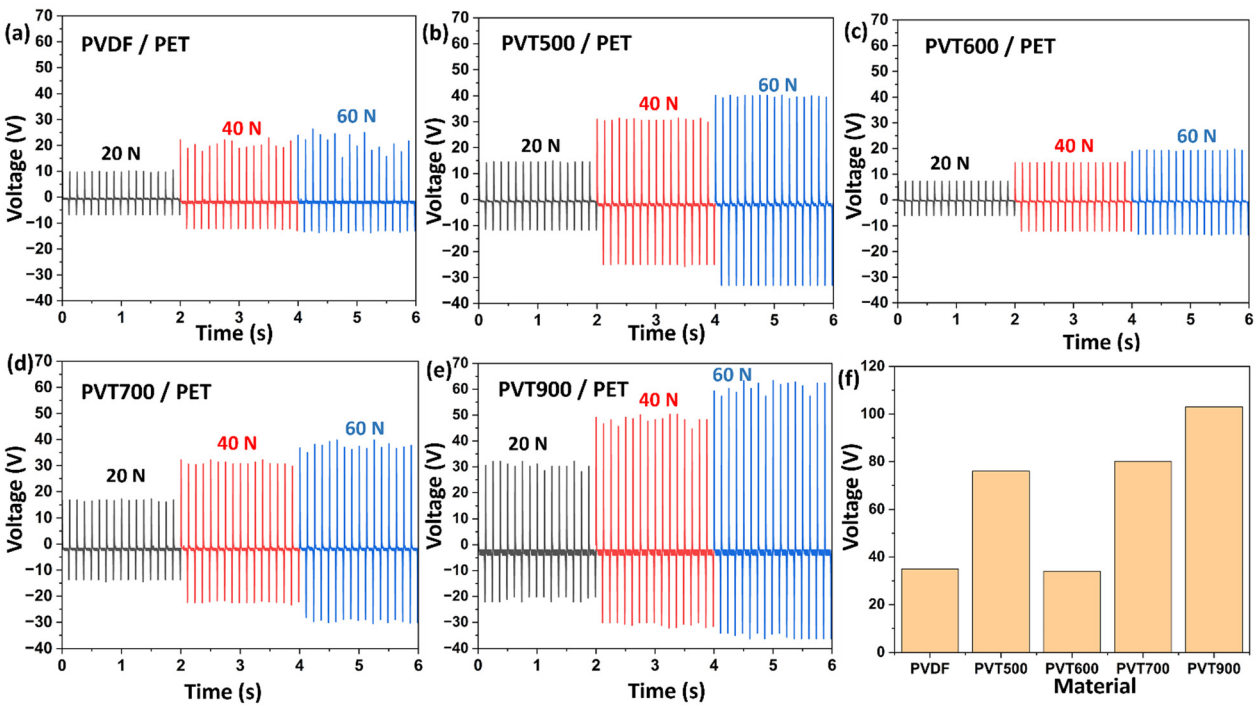

Fig. 8 Voltage output of PVDF and PVDF–TiO_2 samples tested by pairing with ITO-coated PET films at contact forces of 20 N, 40 N, and 60 N and a frequency of 8 Hz using a force impactor. (a) Pristine PVDF film, (b) PVT500 film, (c) PVT600 film, (d) PVT700 film, (e) PVT900 film, and (f) graphical comparison of peak-to-peak voltage values.

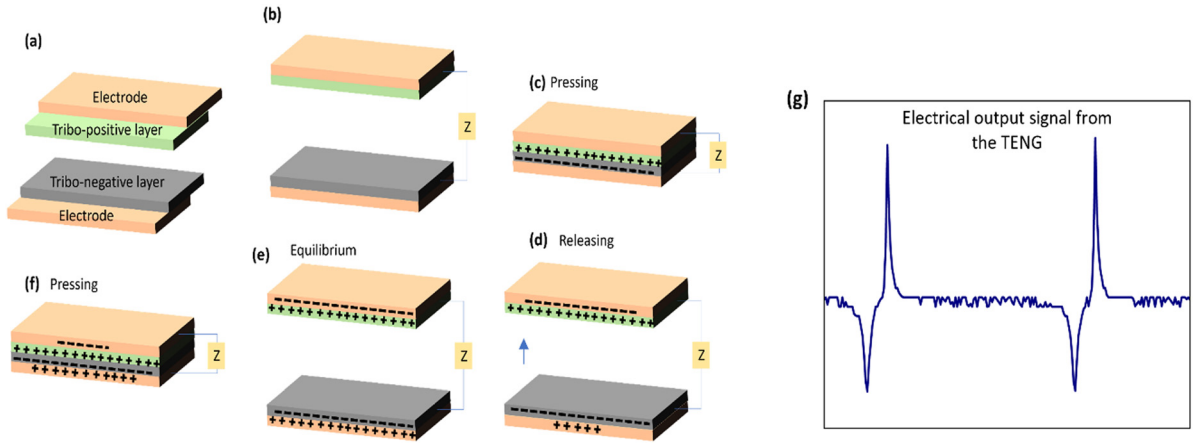

Fig. 9 (a)–(f) Schematic representation of the principle of operation of the contact-separation mode TENG and (g) the electrical output signal obtained from the of the vertical contact–separation TENG tests.

peak–peak voltage value as compared to that of PVT600. However, the highest value of peak–peak voltage was observed for PVT900 which has TiO_2 samples with a complete rutile phase (Fig. 2(e)). This trend is repeated in the case of 20 N and 40 N force conditions as well. This shows that the enhancement of the voltage output of PVDF is greater in single phase TiO_2 added PVDF than a mixed phase TiO_2 incorporated PVDF, and also, the pure rutile phase of TiO_2 enhances the triboelectric property of PVDF more than the pure anatase phase and the mixed phase TiO_2.

The mode of operation of PVDF–TiO_2/PET TENG can be explained based on the vertical contact separation working mode illustrated in Fig. 9. Initially, the surfaces were separated from each other and at this point, they are electrically neutral. When the two surfaces come into contact with each other, the transfer of electrons is expected to occur from the PET film to

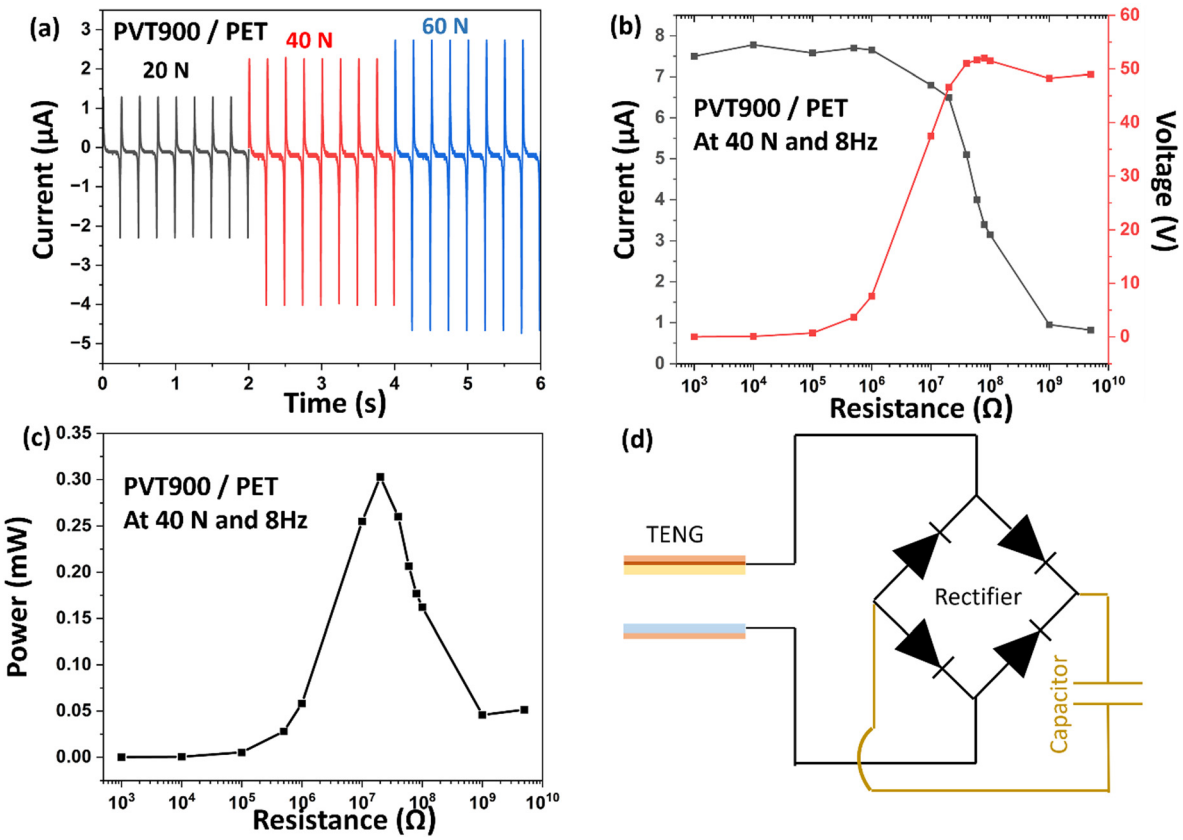

Fig. 10 (a) Comparison of current output generated by PVT900 paired with PET at contact forces 20 N, 40 N and 60 N at a frequency of 8 Hz. (b) Load matching voltage and current values and (c) load matching peak power values obtained for PVT900 at 40 N 8 Hz under external load resistance ranging from 1 KΩ to 5 GΩ. (d) Diagram of the circuit used for capacitor charging with the power output from the developed TENG.

the tribonegative PVDF film due to contact electrification. This results in the generation of positive charges on the PET surface and negative charges on the PVDF surface. In the next instance when the surfaces separated from each other, a potential difference is induced between the back electrodes attached to PVDF and PET films. Also due to electrostatic induction, charges with opposite polarity develop on the electrodes. During the next cycle of contact, the tribo-layers approach each other bringing the potential difference down to zero and causing the current to flow in the opposite direction to that in the previous cycle. Repeated contact-separation cycles result in the flow of current with a change in direction in the alternative cycles between the electrodes leading to an AC voltage in the external circuit.[44]

The current output of PVT900 paired with PET under contact separation mode at forces 20 N, 40 N and 60 N at 8 Hz frequency are shown in Fig. 10(a). An output of ~1.5 μA, 2.5 μA, and 3 μA are obtained at forces 20 N, 40 N and 60 N respectively. The voltage and current output against external load matching of the PVT900 TENG was performed and measured over a range of load resistances (1 KΩ–5 GΩ) at a constant cyclic force of 40 N and a frequency of 8 Hz. Also, the peak power of the TENG device at different applied external loads was measured by the equation[45] as

$$P = \frac{I^2 R}{A} \tag{4}$$

The fabricated PVDF–TiO_2 TENG (PVT900) paired with PET was subjected to a continuous loading of a constant force of 40 N at a frequency of 8 Hz for 2000 s (16 000 contact separation cycles) to evaluate the stability of its output (Fig. 11(a)). A peak-to-peak voltage of ~56 V was obtained without any considerable variation in the voltage throughout the testing cycle indicating the stability of the TENG device over long working cycles. The PVT900 sample paired with PET under contact separation mode at a contact force of 40 N at a frequency of 8 Hz was applied to perform the capacitor charging and light emitting diodes (LED) lighting. Fig. 11(c) shows the photographic image of the force impactor rig used for the TENG studies.

The self-powering capability of the TENG was estimated by charging different commercial capacitors with capacitances of 1, 4.7, 10, 22 and 47 μF using the PVT900 sample. Fig. 11(b) shows that the 1 μF capacitor can be charged up to ~2.5 V,

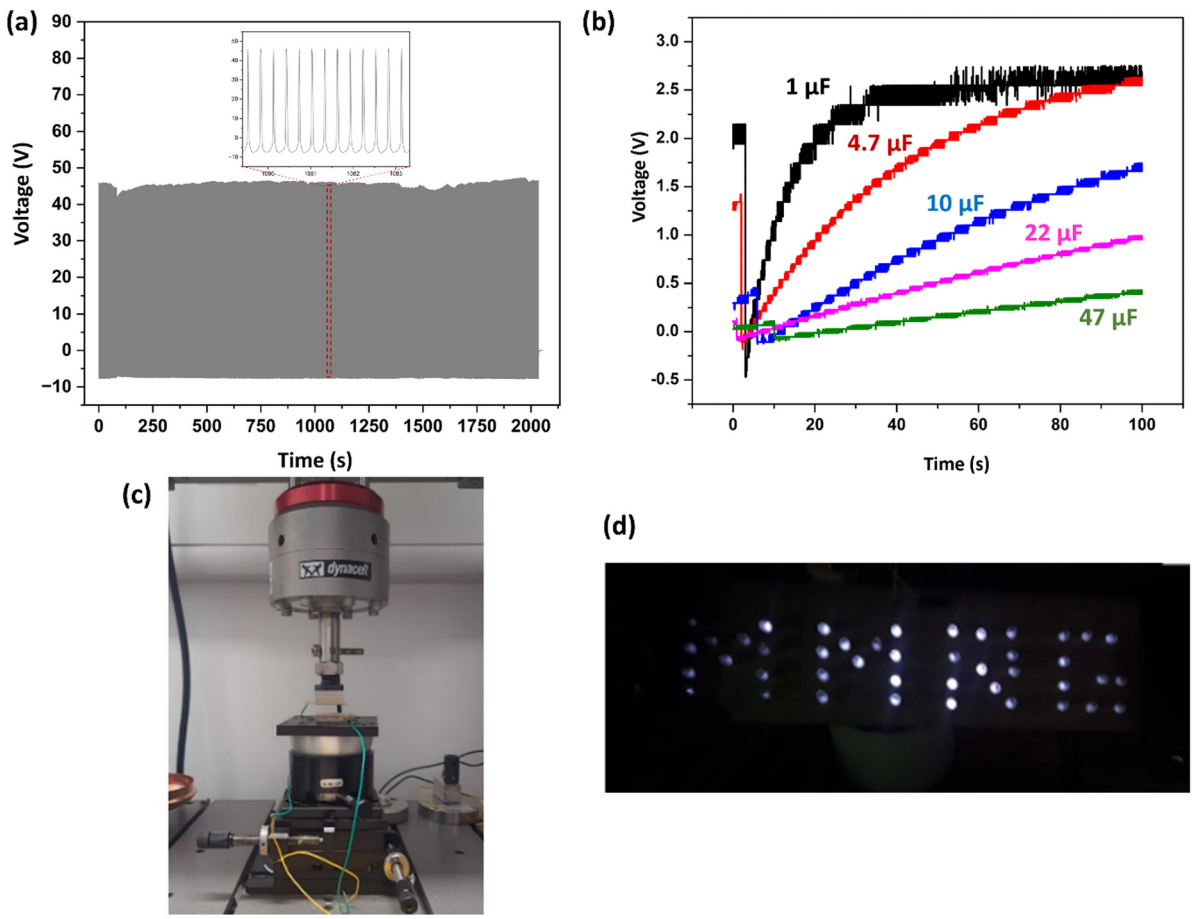

Fig. 11 (a) Stability of the voltage output signal from TENG over time and (b) charging of a range of capacitors using the TENG in contact separation mode at a constant force of 40 N and frequency of 8 Hz. (c) Photographic image of the force impactor rig used for the TENG studies. (d) Demonstration of the energy harvesting ability of TENG by illuminating 40 LEDs connected in series forming the word 'MMRG'.

Table 1 Comparison of the electrical output of the TENG device with the TENGs with similar research methods reported in the literature

TENG system	Material(s) used	Output performance	Application(s)	Ref.
Electrospun flexible membrane based TENG	PVDF–ZnO NWs/nylon-ZnO NWs	Power density = 3.0 W m^{-2}	Mechanical energy harvesting	17
Phase inversion enabled film based TENG	PVDF–TiO_2/cellulose acetate	Output voltage ~60 V Output current ~450 nA	Benzene monitoring system	21
Droplet based TENG	PVDF – lead free potassium sodium niobate (KNN-PVDF)	Output voltage = 1.56 V Output current = 9.91 μA	Energy harvesting using sea waves	47
Electrospun TENG	Copper oxide (CuO) nanoparticles doped PVDF	Output voltage = 7.5 V	Wearable and biomedical applications	48
Thermally drawn polymer nanocomposite fibre based TENG	Graphene integrated PVDF	Output voltage ~35 V Output current ~20 μA	Application in extreme environmental conditions	43
Stretchable, transparent TENG	MXene nanosheets, silver nanowires, PU, PDMS	V_{oc} = 38 V Current density = 1.67 mA m^{-2}	Motion sensor	49
Fully stretchable and durable TENG	Au nanosheets embedded PDMS matrix	V_{oc} = 98.9 V I_{sc} = 2.8 μA	Medical diagnostics and wireless sensors	50
Highly flexible TENGs	TiO_2 nanorod arrays, titanium substrate	V_{oc} = 40 V Current density = 1 mA cm^{-2}	Biosensors, photo detectors	51
Electroactive phase dependant PVDF–TiO_2 nanocomposite based TENG	PVDF–TiO_2/ITO coated PET	Output voltage ~ 60 V Output current ~ 3 μA	Mechanical energy harvesting	This work

4.7 μF capacitor up to ~2.5 V, 10 μF capacitor up to ~1.5 V, 22 μF capacitor up to ~1.0 V and 47 μF capacitor up to ~0.45 V within 100 seconds of charging. The rectifier circuit used to charge the capacitors using the TENG is shown in Fig. 10(d). Thus, the fabricated TENG can be used to power electronic devices by storing the generated output in a capacitor. Additionally, as a demonstration of the TENG ability of the fabricated device, 46 LEDs connected in series were illuminated as shown in Fig. 11(d) and Fig. S5 (ESI†). One of the main limitations of TENGs is their low current output (microampere range) owing to the high internal impedance in them (mega Ohm range). Those limitations are also observed in the TENG shown in the current study. The maximum current output obtained was approximately 3 μA (Fig. 10(a)) and the internal impedance of TENG was observed to be in the mega Ohm range from the load-matching studies (Fig. 11(b)).

Considerable change in the TENG output performance was observed based on the crystalline phase of TiO_2 nanoparticles incorporated in the PVDF matrix. A gradual change in the crystalline phase of TiO_2 was observed by calcining the samples over a range of temperatures from 500 °C to 1000 °C and the percentage of the rutile phase increased with an increase in the calcination temperature of the TiO_2 nanoparticles.[29,46] The difference in crystalline phase modulation of PVDF based on the crystalline phase of the incorporated TiO_2 was observed from the XRD and FT-IR analysis of the films.[43] It was shown that the electroactive phase (EA) percentage of PVT500 and PVT900 films with pure anatase and pure rutile TiO_2 respectively was higher than that of the mixed phase TiO_2 incorporated PVDF films. This change in the EA phase content of PVDF–TiO_2 films influenced the electrical output of the PVDF–TiO_2 films when paired with PET. The pristine PVDF film showed a peak-to-peak voltage of ~35 V and this increased up to ~77 V for PVT500 films which have anatase phase TiO_2 nanoparticles. The peak-to-peak voltage of PVT600 which has a mix of anatase (52.4%) and rutile (47.6%) phase was found to be considerably decreased to ~33 V. This shows that apart from the crystallinity and percentage loading of TiO_2, the crystalline phase of TiO_2 has an impact on the TENG output of PVDF–TiO_2 composites.[21,22] This was further confirmed by evaluating the voltage output of PVT700 which also had a mixed phase of TiO_2 but with a higher percentage of rutile phase. The peak-to-peak voltage value of PVT700 increased up to ~82 V. The maximum peak-to-peak voltage was attained for PVT900 (~105 V) with a pure rutile phase TiO_2. From these results, it can be inferred that the rutile phase of TiO_2 imparts a higher content of EA phase in PVDF–TiO_2 nanocomposites compared to that of other phases. Owing to this, the TENG output of rutile phase TiO_2 containing PVDF is higher than that of anatase and mixed phase containing TiO_2 nanoparticles. This study showed comparable voltage output to the PVDF nanocomposite-based and other flexible and stretchable TENGs reported in the literature (Table 1). Moreover, the fabrication of the proposed TENG involves low-cost techniques and materials, making the TENG worth approximately 50 EUR. A simple spin coating method was used to prepare the tribonegative film (Section 2.3), and low-cost materials such as Kapton tape and acrylic sheets were used to assemble this 2.5 cm^2 TENG (Section 2.4). However, in TENGs the comparison of electrical output with similar reported TENGs is not a reliable practice for some obvious reasons. Firstly, the output will vary depending on the properties of the opposite contact layer used as well. Also, the conditions of contact separation, force and frequency at which the TENGs were analysed, humidity conditions *etc.* will affect the output. Furthermore, concerning the force impactor instrument/rig used for testing, the contact mechanics of the TENG will vary from rig to rig as well as due to the two different materials involved in the operation of TENG.

4. Conclusions

The impact of crystallinity and crystalline phase of TiO_2 nanoparticles on the crystalline phase modification of the PVDF

matrix and its effects on the TENG property of PVDF–TiO_2 nanocomposites was investigated in this study. TiO_2 nanoparticles with pure anatase, purely rutile and a mix of anatase and rutile phases were synthesized and incorporated into the PVDF matrix. The manipulation of the electroactive phase of PVDF was found to vary depending on the change in the crystalline phase of TiO_2 present in the composite. Composite film containing purely rutile TiO_2 showed the maximum enhancement in the electroactive phase and the same film showed the maximum surface roughness as well. On pairing with PET under contact separation mode and when tested at different conditions of force at a constant frequency, it was observed that the pure rutile TiO_2 containing sample showed the maximum electrical output. Moreover, the electroactive phase analysis, surface roughness analysis and the electrical output performance of the films show that the single crystalline phase TiO_2 containing PVDF–TiO_2 composites show higher output than that of TiO_2 with a mix of anatase and rutile phase. These findings are expected to act as a guide when tuning the PVDF electroactive phase by incorporating it to improve TENG performance.[52,53]

Author contributions

Irthasa Aazem: methodology; investigation; formal analysis; conceptualization; writing – original draft. Charchit Kumar: investigation, formal analysis; writing – review and editing. Ryan Walden: investigation, writing – review and editing. Aswathy Babu: validation, writing – review and editing. Amit Goswami: investigation; methodology; writing – review and editing. Steven Hinder: investigation. Gaurav Khandelwal: investigation, writing – review and editing. Daniel Mulvihill: project administration, resources. Gerard McGranaghan: writing – review and editing; resources, supervision. Suresh C. Pillai: supervision; funding acquisition; validation; conceptualization, writing – review and editing.

Data availability

The data supporting this article have been included as part of the ESI.†

Conflicts of interest

There are no conflicts to declare.

Acknowledgements

This work was funded by Research Ireland (SFI-20/EPSRC/3710) under the Research Ireland-EPSRC Joint Funding of Research and the Connacht-Ulster Alliance (CUA) bursary in Sligo. We also acknowledge the support from the UK Engineering and Physical Sciences Research Council (EPSRC) through grant Ref. EP/V003380/1 (''Next Generation Energy Autonomous Textile Fabrics based on Triboelectric Nanogenerators''). Additionally, we extend our gratitude to Dr Barry Brennan for his assistance in analyzing XPS data. For the purpose of open access, the authors have applied a Creative Commons Attribution (CC BY) licence to any Author Accepted Manuscript version arising'.

References

1 G. Min, Y. Xu, P. Cochran, N. Gadegaard, D. M. Mulvihill and R. Dahiya, Nano Energy Origin of the contact force-dependent response of triboelectric nanogenerators, *Nano Energy*, 2021, **83**, 105829, DOI: 10.1016/j.nanoen.2021.105829.
2 T. Cheng, Q. Gao and Z. L. Wang, The Current Development and Future Outlook of Triboelectric Nanogenerators: A Survey of Literature, *Adv. Mater. Technol.*, 2019, **4**(3), 1–7.
3 S. Bairagi, Shahid-ul-Islam, M. Shahadat, D. M. Mulvihill and W. Ali, Mechanical energy harvesting and self-powered electronic applications of textile-based piezoelectric nanogenerators: A systematic review, *Nano Energy*, 2023, **111**, 108414, DOI: 10.1016/j.nanoen.2023.108414.
4 S. Zhao, J. Li, D. Cao, G. Zhang, J. Li and K. Li, *et al.*, Recent Advancements in Flexible and Stretchable Electrodes for Electromechanical Sensors: Strategies, Materials, and Features, *ACS Appl. Mater. Interfaces*, 2017, **9**(14), 12147–12164.
5 F. R. Fan, Z. Q. Tian and Z. Lin Wang, Flexible triboelectric generator, *Nano Energy*, 2012, **1**(2), 328–334, DOI: 10.1016/j.nanoen.2012.01.004.
6 Z. L. Wang and J. Song, Piezoelectric nanogenerators based on zinc oxide nanowire arrays, *Science*, 2006, **312**(5771), 242–246.
7 J. Liu, L. Zhang, N. Wang and C. Li, Highly stretchable and transparent triboelectric nanogenerator based on multilayer structured stable electrode for self-powered wearable sensor, *Nano Energy*, 2020, **78**, 105385, DOI: 10.1016/j.nanoen.2020.105385.
8 K. Parida, V. Kumar, W. Jiangxin, V. Bhavanasi, R. Bendi and P. S. Lee, Highly Transparent, Stretchable, and Self-Healing Ionic-Skin Triboelectric Nanogenerators for Energy Harvesting and Touch Applications, *Adv. Mater.*, 2017, **29**(37), 1–8.
9 F. Yi, J. Wang, X. Wang, S. Niu, S. Li and Q. Liao, *et al.*, Stretchable and Waterproof Self-Charging Power System for Harvesting Energy from Diverse Deformation and Powering Wearable Electronics, *ACS Nano*, 2016, **10**(7), 6519–6525.
10 Z. Wen, M. H. Yeh, H. Guo, J. Wang, Y. Zi and W. Xu, *et al.*, Self-powered textile for Wearable electronics by hybridizing fiber-shaped nanogenerators, solar cells, and supercapacitors, *Sci. Adv.*, 2016, **2**(10), 1–9.
11 H. J. Yang, J. W. Lee, S. H. Seo, B. Jeong, B. Lee and W. J. Do, *et al.*, Fully stretchable self-charging power unit with micro-supercapacitor and triboelectric nanogenerator based on oxidized single-walled carbon nanotube/polymer electrodes, *Nano Energy*, 2021, **86**, 106083, DOI: 10.1016/j.nanoen.2021.106083.
12 X. Wang, D. Zhang, H. Zhang, L. Gong, Y. Yang and W. Zhao, *et al.*, *In situ* polymerized polyaniline/MXene (V2C) as building blocks of supercapacitor and ammonia sensor self-powered by electromagnetic-triboelectric hybrid

generator, *Nano Energy*, 2021, **88**, 106242, DOI: 10.1016/j.nanoen.2021.106242.

13 J. Dong, S. Huang, J. Luo, J. Zhao, F. R. Fan and Z. Q. Tian, Supercapacitor-Inspired Triboelectric Nanogenerator Based on Electrostatic Double Layer, *Nano Energy*, 2022, **95**, 106971, DOI: 10.1016/j.nanoen.2022.106971.

14 J. Sun, X. Pu, M. Liu, A. Yu, C. Du and J. Zhai, *et al.*, Self-Healable, Stretchable, Transparent Triboelectric Nanogenerators as Soft Power Sources, *ACS Nano*, 2018, **12**(6), 6147–6155.

15 Z. Wu, T. Cheng and Z. L. Wang, Self-powered sensors and systems based on nanogenerators, *Sensors*, 2020, **20**(10), 1–46.

16 A. Mahapatra, R. S. Ajimsha, D. Deepak, Sumit, R. Aggarwal and S. Kumar, *et al.*, Textile-integrated MoS2-PDMS single electrode triboelectric nanogenerator for vibrational energy harvesting and biomechanical motion sensing, *Nano Energy*, 2023, **116**, 108829, DOI: 10.1016/j.nanoen.2023.108829.

17 X. Pu, J. W. Zha, C. L. Zhao, S. B. Gong, J. F. Gao and R. K. Y. Li, Flexible PVDF/nylon-11 electrospun fibrous membranes with aligned ZnO nanowires as potential triboelectric nanogenerators, *Chem. Eng. J.*, 2020, **398**(30), 125526, DOI: 10.1016/j.cej.2020.125526.

18 D. L. Vu and K. K. Ahn, Triboelectric Enhancement of Polyvinylidene Fluoride Membrane Using Magnetic Nanoparticle for Water-Based Energy Harvesting, *Polymers*, 2022, **14**(8), 1547, DOI: 10.3390/polym14081547.

19 L. Jin, X. Xiao, W. Deng, A. Nashalian, D. He and V. Raveendran, *et al.*, Manipulating Relative Permittivity for High-Performance Wearable Triboelectric Nanogenerators, *Nano Lett.*, 2020, **20**(9), 6404–6411.

20 L. Shi, H. Jin, S. Dong, S. Huang, H. Kuang and H. Xu, *et al.*, High-performance triboelectric nanogenerator based on electrospun PVDF-graphene nanosheet composite nanofibers for energy harvesting, *Nano Energy*, 2021, **80**, 105599, DOI: 10.1016/j.nanoen.2020.105599.

21 G. Khandelwal, A. Chandrasekhar, R. Pandey, N. P. Maria Joseph Raj and S. J. Kim, Phase inversion enabled energy scavenger: A multifunctional triboelectric nanogenerator as benzene monitoring system, *Sens. Actuators, B*, 2019, **282**, 590–598, DOI: 10.1016/j.snb.2018.11.110.

22 M. M. Alam, A. Sultana and D. Mandal, Biomechanical and Acoustic Energy Harvesting from TiO2 Nanoparticle Modulated PVDF Nanofiber Made High Performance Nanogenerator, *ACS Appl. Energy Mater.*, 2018, **1**(7), 3103–3112.

23 M. Peng, K. Li, B. Huang and J. Cheng, PVDF promotes TiO_2 dispersion to obtain composite films with high dielectric constant and low loss, *High Perform. Polym.*, 2022, **34**(1), 95–104.

24 H. Hong, S. A. Song and S. S. Kim, Phase transformation of poly(vinylidene fluoride)/TiO_2 nanocomposite film prepared by microwave-assisted solvent evaporation: An experimental and molecular dynamics study, *Compos. Sci. Technol.*, 2020, **199**, 108375, DOI: 10.1016/j.compscitech.2020.108375.

25 S. C. Pillai, P. Periyat, R. George, D. E. McCormack, M. K. Seery and H. Hayden, *et al.*, Synthesis of high-temperature stable anatase TiO_2 photocatalyst, *J. Phys. Chem. C*, 2007, **111**(4), 1605–1611.

26 D. Dodoo-Arhin, F. P. Buabeng, J. M. Mwabora, P. N. Amaniampong, H. Agbe and E. Nyankson, *et al.*, The effect of titanium dioxide synthesis technique and its photocatalytic degradation of organic dye pollutants, *Heliyon*, 2018, **4**(7), e00681, DOI: 10.1016/j.heliyon.2018.e00681.

27 C. Byrne, L. Moran, D. Hermosilla, N. Merayo, Á. Blanco and S. Rhatigan, *et al.*, Effect of Cu doping on the anatase-to-rutile phase transition in TiO_2 photocatalysts: Theory and experiments, *Appl. Catal., B*, 2019, **246**, 266–276.

28 C. Kumar, J. Perris, S. Bairagi, G. Min, Y. Xu and N. Gadegaard, *et al.*, Multiscale in-situ quantification of the role of surface roughness and contact area using a novel Mica-PVS triboelectric nanogenerator, *Nano Energy*, 2023, **107**, 108122, DOI: 10.1016/j.nanoen.2022.108122.

29 T. Theivasanthi and M. Alagar, *Titanium dioxide (TiO_2) Nanoparticles XRD Analyses: An Insight*, 2013, Available from: https://arxiv.org/abs/1307.1091.

30 B. Erdem, R. A. Hunsicker, G. W. Simmons, E. David Sudol, V. L. Dimonie and M. S. El-Aasser, XPS and FTIR surface characterization of TiO_2 particles used in polymer encapsulation, *Langmuir*, 2001, **17**(9), 2664–2669.

31 N. Saikumari, S. M. Dev and S. A. Dev, Effect of calcination temperature on the properties and applications of bio extract mediated titania nano particles, *Sci. Rep.*, 2021, **11**(1), 1–17, DOI: 10.1038/s41598-021-80997-z.

32 K. P. Priyanka, S. Joseph, A. Sunny and T. Varghese, Effect of high energy electron beam irradiation on the optical properties of nanocrystalline TiO_2, *Nanosyst.: Phys., Chem., Math.*, 2013, **4**(2), 218–224.

33 D. A. H. Hanaor and C. C. Sorrell, Review of the anatase to rutile phase transformation, *J. Mater. Sci.*, 2011, **46**(4), 855–874.

34 N. Rathore, A. Kulshreshtha, R. K. Shukla and D. Sharma, Study on morphological, structural and dielectric properties of sol-gel derived TiO_2 nanocrystals annealed at different temperatures, *Phys. B*, 2020, **582**, 411969, DOI: 10.1016/j.physb.2019.411969.

35 R. A. Spurr and H. Myers, Quantitative Analysis of Anatase-Rutile Mixtures with an X-Ray Diffractometer, *Anal. Chem.*, 1957, **29**(5), 760–762.

36 H. Parangusan, D. Ponnamma and M. Al Ali Almaadeed, Toward High Power Generating Piezoelectric Nanofibers: Influence of Particle Size and Surface Electrostatic Interaction of Ce–Fe_2O_3 and Ce–Co_3O_4 on PVDF, *ACS Omega*, 2019, **4**(4), 6312–6323.

37 C. Fu, H. Zhu, N. Hoshino, T. Akutagawa and M. Mitsuishi, Interfacial nanostructuring of poly(vinylidene fluoride) homopolymer with predominant ferroelectric phases, *Langmuir*, 2020, **36**(46), 14083–14091.

38 R. I. Haque, R. Vié, M. Germainy, L. Valbin, P. Benaben and X. Boddaert, Inkjet printing of high molecular weight PVDF-TrFE for flexible electronics, *Flexible Printed Electron.*, 2016, **1**(1), 015001, DOI: 10.1088/2058-8585/1/1/015001.

39 K. Oumghar, N. Chakhchaoui, R. Farhane, A. Eddiai, M. Meddad and O. Cherkaoui, *et al.*, Enhanced piezoelectric

properties of PVdF-HFP/PZT nanocomposite for energy harvesting application, *IOP Conf. Ser.: Mater. Sci. Eng.*, 2020, **827**(1), 6–11.

40 Z. Yin, B. Tian, Q. Zhu and C. Duan, Characterization and application of PVDF and its copolymer films prepared by spin-coating and Langmuir-Blodgett method, *Polymers*, 2019, **11**(12), 2033, DOI: 10.3390/polym11122033.

41 A. Issa, M. Al-Maadeed, A. Luyt, D. Ponnamma and M. Hassan, Physico-Mechanical, Dielectric, and Piezoelectric Properties of PVDF Electrospun Mats Containing Silver Nanoparticles, *C*, 2017, **3**(4), 30.

42 Z. Arif, N. K. Sethy, L. Kumari, P. K. Mishra and B. Verma, Antifouling behaviour of PVDF/TiO_2 composite membrane: a quantitative and qualitative assessment, *Iran. Polym. J.*, 2019, **28**(4), 301–312, DOI: 10.1007/s13726-019-00700-y.

43 M. S. B. Sadeque, M. Rahman, M. M. Hasan and M. Ordu, Graphene Nanoplatelet Integrated Thermally Drawn PVDF Triboelectric Nanocomposite Fibers for Extreme Environmental Conditions, *Adv. Electron. Mater.*, 2024, **10**(4), 2470015, DOI: 10.1002/aelm.202470015.

44 S. Bairagi, G. Khandelwal, X. Karagiorgis, S. Gokhool, C. Kumar and G. Min, *et al.*, High-Performance Triboelectric Nanogenerators Based on Commercial Textiles: Electrospun Nylon 66 Nanofibers on Silk and PVDF on Polyester, *ACS Appl. Mater. Interfaces*, 2022, **14**(39), 44591–44603.

45 Y. Zhao, W. Yang, Y. Zhou, Y. Chen, X. Cao and Y. Yang, *et al.*, Effect of crystalline phase on the dielectric and energy storage properties of poly(vinylidene fluoride), *J. Mater. Sci.: Mater. Electron.*, 2016, **27**(7), 7280–7286.

46 C. Langa, Z. N. Tetana and N. C. Hintsho-Mbita, Effect of calcination temperature on the synthesis of TiO_2 nanoparticles from Sutherlandia frutescence for the degradation of Congo red dye and antibiotics ciproflaxin and sulfamethoxazole, *Chem. Phys. Impact*, 2023, **7**, 100389, DOI: 10.1016/j.chphi.2023.100389.

47 B. Sharma, R. Gupta, A. Sharma, A. Chowdhuri and M. Tomar, Fabrication of droplet based triboelectric nanogenerators (DB-TENGs) using lead free KNN-PVDF nanocomposite, *Chem. Phys. Impact*, 2025, **10**, 100813, DOI: 10.1016/j.chphi.2025.100813.

48 B. Amrutha, G. Prasad, P. Sathiyanathan, M. S. Reza, H. Kim and M. Pathak, *et al.*, Fabrication of CuO-NP-Doped PVDF Composites Based Electrospun Triboelectric Nanogenerators for Wearable and Biomedical Applications, *Polymers*, 2023, **15**(11), 2442, DOI: 10.3390/polym15112442.

49 J. Liu, L. Zhang, N. Wang and C. Li, Highly stretchable and transparent triboelectric nanogenerator based on multilayer structured stable electrode for self-powered wearable sensor, *Nano Energy*, 2020, **78**, 105385, DOI: 10.1016/j.nanoen.2020.105385.

50 G. H. Lim, S. S. Kwak, N. Kwon, T. Kim, H. Kim and S. M. Kim, *et al.*, Fully stretchable and highly durable triboelectric nanogenerators based on gold-nanosheet electrodes for self-powered human-motion detection, *Nano Energy*, 2017, **42**, 300–306, DOI: 10.1016/j.nanoen.2017.11.001.

51 R. Mohammadpour, Flexible Triboelectric Nanogenerator Based on High Surface Area TiO_2 Nanotube Arrays, *Adv. Eng. Mater.*, 2018, **20**(5), 1–7.

52 Y. F. Chen, C. Y. Lee, M. Y. Yeng and H. T. Chiu, The effect of calcination temperature on the crystallinity of TiO_2 nanopowders, *J. Cryst. Growth*, 2003, **247**(3–4), 363–370.

53 X. Cai, T. Lei, D. Sun and L. Lin, A critical analysis of the α, β and γ phases in poly(vinylidene fluoride) using FTIR, *RSC Adv.*, 2017, **7**(25), 15382–15389.